Universal scaling of the dynamic BKT transition in quenched 2D Bose gases

Shinichi Sunami[1*], Vijay Pal Singh[2,3], David Garrick[1], Abel Beregi[1], Adam J. Barker[1], Kathrin Luksch[1], Elliot Bentine[1], Ludwig Mathey[4,5], Christopher J. Foot[1]

[1]Clarendon Laboratory, University of Oxford; Oxford OX1 3PU, United Kingdom

[2]Institut für Theoretische Physik, Leibniz Universität Hannover; Appelstraße 2, 30167 Hannover, Germany

[3]Quantum Research Centre, Technology Innovation Institute, Abu Dhabi, UAE

[4]Zentrum für Optische Quantentechnologien and Institut für Laserphysik, Universität Hamburg; 22761 Hamburg, Germany

[5]The Hamburg Centre for Ultrafast Imaging; Luruper Chaussee 149, Hamburg 22761, Germany

[*]Corresponding author. Email: shinichi.sunami@physics.ox.ac.uk

The understanding of non-equilibrium dynamics in many-body quantum systems is a fundamental issue in statistical physics. Experiments that probe universal properties of these systems can address such foundational questions. Here we report the measurement of universal dynamics triggered by a quench from the superfluid to normal phase across the Berezinskii-Kosterlitz-Thouless transition in a two-dimensional (2D) Bose gas. We reduce the density by splitting the 2D gas in two and probe the subsequent relaxation dynamics. We measure local phase fluctuations, by matter-wave interferometry, to determine the phase correlation function and vortex density, and show that their time evolution obeys universal scaling laws. This conclusion is supported by classical-field simulations and interpreted using real-time renormalization group the-

ory.

Link to the final published version

https://www.science.org/doi/10.1126/science.abq6753

One-sentence Summary

A quenched 2D quantum gas shows universal non-equilibrium vortex dynamics in agreement with real-time renormalization-group theory.

Main Text

The relaxation dynamics of a many-body system that is quenched out of equilibrium displays a wide range of scenarios, from simple exponential decay to relaxation via metastable or prethermalized states (*1, 2*), including phenomena such as pattern formation (*3*), and the absence of thermalization (*4*). Systems that are quenched across a phase transition are particularly intriguing because of their universal self-similar behavior, expected in systems as diverse as superfluid helium (*5*), liquid crystals (*6*), biological cell membranes (*7*), the early universe (*8*), and cold atoms (*9, 10*). There are numerous theoretical challenges in the treatments of non-equilibrium dynamics, see e.g. (*11*), and this motivates in-depth experimental studies to guide and test theories.

For this purpose, ultracold gases have emerged as a platform of unprecedented control and tunability, which serve as quantum simulators for the investigation of many-body dynamics. This has led to the observation of Kibble-Zurek (KZ) scaling (*12–15*) and universal scaling laws (*16–18*) following a quench. Despite theoretical interest (*19–21*), universal critical dynamics in non-equilibrum continuous 2D quantum gases remain elusive because of the lack of precise experimental probes. We show how fluctuations of the many-body 2D system can be probed directly through the extension of local matter-wave interferometry (*22*), similar to that

previously utilised to probe the local phase fluctuations of near-integrable 1D systems (*1, 2*). A feature of 2D is that, unlike 1D systems, they exhibit phase transitions with associated critical phenomena. An especially interesting case is the critical dynamics across the Berezinskii-Kosterlitz-Thouless (BKT) transition (*23–25*) when the system is quenched from the superfluid to the normal phase, the opposite of commonly employed quenches from disordered to ordered phase. Real-time renormalization-group (RG) theory and truncated Wigner simulations (*19*) predict that the relaxation occurs via a reverse-Kibble-Zurek type mechanism in which delayed vortex proliferation results in a metastable supercritical phase. For equilibrium systems, the BKT transition is driven by the unbinding of vortex-antivortex pairs (*22, 26*), underscoring the topological nature of the transition. This transition is characterized by a change of the functional form of the correlation function from a power law deep in the superfluid regime, $g_1(\boldsymbol{r}, \boldsymbol{r}') = \langle \Psi(\boldsymbol{r})^\dagger \Psi(\boldsymbol{r}') \rangle \propto |\boldsymbol{r} - \boldsymbol{r}'|^{-\eta}$, to exponential deep in the normal regime $g_1(\boldsymbol{r}, \boldsymbol{r}') \propto e^{-|\boldsymbol{r}-\boldsymbol{r}'|/r_0}$, where $\Psi(\boldsymbol{r})$ is the bosonic field operator at position vector $\boldsymbol{r}$, η is the algebraic exponent and r_0 is a correlation length. A similar change of the functional form of the single-particle correlation function is also expected for the dynamical BKT transition. However, it is expected to occur as a smooth crossover between the two phases (*19, 27*).

Here, we study the critical dynamics across the BKT transition by quenching a 2D Bose gas from the superfluid to the normal phase by splitting it in two. Using spatially-resolved matter-wave interferometry, we measure the first-order correlation function and vortex density to analyze their relaxation dynamics. We find that relaxation occurs via a two-step process, involving phonon relaxation and then dynamical vortex proliferation. We demonstrate universal scaling laws for the algebraic exponent and vortex density by performing measurements at different initial conditions. Both real-time RG theory (*19, 28*) and classical-field simulations are in good agreement with our measurements.

Our experiments begin with a single pancake-shaped quasi-2D Bose gas in the superfluid

regime, consisting of $N \approx 9 \times 10^4$ atoms of ^{87}Rb at reduced temperatures in the range $\tilde{T} = 0.34 - 0.5$. $\tilde{T} \equiv T/T_0$ is the ratio of the initial temperature T and the critical temperature $T_0 = \sqrt{6N}(\hbar\omega_r/\pi k_B) \approx 120$ nK of a non-interacting trapped gas (*29*), where $\omega_r/2\pi = 11$ Hz is the radial trapping frequency and k_B is the Boltzmann constant. The quench is implemented by a rapid splitting of the system in a multiple-RF dressed potential (*27, 30–32*), as illustrated in Fig. 1A, which results in a pair of decoupled clouds each with atom number $N' = N/2$ trapped in the two minima of a double-well potential. Each well has a vertical trap frequency of $\omega_z/2\pi = 1$ kHz hence the dimensionless 2D interaction strength is $\tilde{g} = \sqrt{8\pi}a_s/\ell_0 = 0.076$ (*27*), where a_s is the 3D scattering length and $\ell_0 = \sqrt{\hbar/(m\omega_z)}$ is the harmonic oscillator length along z for an atom of mass m. The initial reduced temperature $\tilde{T}$ is chosen to be close to the equilibrium critical point at $\tilde{T}_{\mathrm{c,eq}} = 0.53$ so that the value after splitting, $\tilde{T}'/\tilde{T} = 1.67$, corresponds to the normal phase (*27*). To investigate the dynamics, we let each cloud evolve independently for time t before performing a time-of-flight expansion of $t_{\mathrm{TOF}} = 16$ ms after which we detect the matter-wave interference that encodes the *in situ* relative phase fluctuation $\phi(x)$ of two clouds along a line that goes through the center of the cloud. Interference images and histograms of spatial phase fluctuations $\Delta\phi$ show stronger fluctuations at long evolution times (Fig. 1C). The dynamics across the BKT transition is expected to be scale-invariant until the bound vortex-antivortex pairs dissociate to disrupt the phase coherence (Fig. 1D).

To analyze the relaxation dynamics, we use the interference pattern to determine both the correlation function and the vortex density (*22*). The phase correlation of the system between two points at locations $x - \overline{x}/2$ and $x + \overline{x}/2$, with spatial separation $\overline{x}$, is determined by $C(x - \overline{x}/2, x + \overline{x}/2) = \mathrm{Re}\left[\frac{1}{N_r}\sum_{j=1}^{N_r} e^{i[\phi_j(x-\overline{x}/2)-\phi_j(x+\overline{x}/2)]}\right]$, where the index j runs over $N_r = 45$ experimental repeats; $C(x - \overline{x}/2, x + \overline{x}/2) = 1$ indicates perfect correlation of phases while $C(x - \overline{x}/2, x + \overline{x}/2) = 0$ denotes uncorrelated phases. For quantitative analysis, we average $C(x - \overline{x}/2, x + \overline{x}/2)$ over x within the region of clear interference fringes to obtain $C(\overline{x})$ (*33*).

In our previous work Ref. (*22*), we identified that $C(\overline{x})$ of equilibrium 2D Bose gases decays algebraically with spatially-varying exponent for inhomogeneous 2D gases in the superfluid regime, in agreement with the prediction based on *local correlation approximation* in Ref. (*34*), while in the normal regime it shows exponential decay.

In Fig. 2A, we show the time evolution of $C(\overline{x})$ after the quench at $t = 0$. Initially, there is almost no spatial correlation decay because the two clouds have nearly identical phases; their phases decouple within $\sim$ 100 ms (*27*). After this, we observe a temporal decay of $C(\overline{x})$ for all $\overline{x}$. At longer times, we observe rapid spatial decay of correlation, indicating vanishing coherence at large distances. To determine the nature of this dynamic transition, we fit $C(\overline{x})$ with the algebraic and exponential functions which are used to characterize the equilibrium BKT transition (*22*). As the system relaxes from the initial superfluid state to the normal state, it is expected that $C(\overline{x})$ will evolve smoothly from algebraic to exponential scaling in the short- and long-time limits, respectively. At intermediate times, both power-law and exponential fitting can be used to extract physical properties of the non-equilibrium state; within the real-time RG picture, non-equilibrium systems in the crossover region are away from the fixed point where there is no direct correspondence to equilibrium systems (*19, 35*). Indeed, at short and intermediate times the spatial decay of the correlation function is compatible with algebraic scaling, including the effect of inhomogeneity of the system, and with exponential scaling for long times (*27*). We identify the crossover time t_c, as the time at which the correlation function becomes better described by exponential scaling rather than algebraic; see Fig. 2B. Even after t_c, the χ^2 values for the power-law model remain small, supporting the description of the system with the power-law exponent η beyond t_c (*27*).

For the dynamic BKT transition, we expect self-similar dynamics with a length scale that depends linearly on time (*19, 36, 37*). Motivated by this, in Fig. 2B we plot the correlation functions with rescaled length $x' = \overline{x}t/t_c$ using $t_c \sim 0.5$ s. This shows convincingly that the

fluctuations in the system only depend on the rescaled parameter x' through a universal function, which we find to be close to the expected function at the equilibrium BKT crossover (Fig. 2B). We find the same behavior independent of the initial condition (temperature) of the system, demonstrating the robustness of the scale-invariant behavior near the critical point (*27*).

At long times, scale invariance is broken by vortex excitations, which results in an emergent length scale $r_0 \approx 1/\sqrt{n_v}$ where n_v is the vortex density (*27*). To demonstrate this, in Fig. 2C we plot the correlation function at long times against the rescaled distance $\tilde{x} = \overline{x}\sqrt{n_v}$ (*37*). We obtain n_v from the occurrence of sudden jumps of phases which indicate the presence of a vortex core (*22, 26, 27*). These transformed correlation functions are nearly time independent, showing that the system can be characterized by the vortex density deep in the normal regime.

Having verified the behavior of the dynamic BKT transition, we now analyze its universal characteristics by varying $\tilde{T}$. The time evolution of the algebraic exponent η, determined via an algebraic fit to $C(\overline{x})$, exhibits a linear increase where the increase is faster for higher $\tilde{T}$ (Fig. 3A). This shows that the dynamics is accelerated at higher $\tilde{T}$ and the system quickly crosses over to the normal phase. This is also reflected in the measurements of the vortex density n_v, showing a faster growth at higher $\tilde{T}$ (Fig. 3B). We find the vortex growth follows a power-law scaling as expected from the RG predictions (*27*). We compare the measurements of η and n_v with the corresponding results of classical-field simulations which give consistent dynamics (Fig. 3, A and B).

To confirm universal scaling, we show η and n_v as a function of scaled time t/t_c in Fig. 3, C and D. The time evolutions for various initial values of $\tilde{T}$ collapse onto a single curve, showing the robustness of dynamical scaling. We find a linear increase of η across $t = t_c$. In equilibrium theory, η scales approximately linearly with temperature in the superfluid regime, i.e. $\eta \propto T/4T_{\mathrm{BKT}}$ (*25*), thus connecting the temperature scale with phase fluctuations. From this linear estimate, we obtain the critical exponent $\eta_c = 0.13(1)$ at $t/t_c = 1$, close to the value

$\eta_c = 0.17(3)$ found for a finite-size equilibrium system with similar experimental parameters (*22*), and different from the value of $\eta_{\mathrm{BKT}} = 0.25$ for the equilibrium BKT transition in the thermodynamic limit. The linear increase of η after $t/t_c = 1$ is a precursor of non-equilibrium superheated superfluid (*28*) as a consequence of a delayed vortex proliferation. From the vortex growth after $t/t_c = 1$ we obtain universal power-law scaling $n_v \propto t^{2\nu}$ with $\nu \sim 1$; this agrees with the RG prediction, as shown below.

We now compare the experimental results with predictions based on the real-time RG equations (*19, 28*). These equations describe the time evolution of parameters characterizing the system from arbitrary non-equilibrium states flowing towards fixed points which represent possible equilibrium states. For the dynamic BKT transition, the real-time RG equations are (*19, 27, 28*)

$$\frac{dg}{dt} = \left(2 - \frac{1}{2\eta}\right)\frac{g}{t}, \tag{1}$$

$$\frac{d\eta}{dt} = \frac{\pi g^2}{16\eta t} + \gamma, \tag{2}$$

where the vortex fugacity g is related to the vortex density by $n_v(t) = n\tilde{g}\exp[(2\ln(g/2))/(2 - 1/(2\eta))]$. n is the mean density within the region of interest used for fringe analysis and $\tilde{g}$ is the interaction strength as defined previously; these parameters also determine the healing length $\xi = 1/\sqrt{n\tilde{g}}$, characterizing the length scale of the vortex cores (*27, 38*). This RG flow derives from the dynamical sine-Gordon model, serving as a dual model for describing the BKT transition and we have added a phenomenological heating term γ to account for the slow trap-induced heating of the system (*27*). For $\eta < 1/4$, the fugacity is strongly suppressed, resulting in a linear dispersion $\omega_k = ck$. As η increases in time, the vortex fugacity becomes relevant and increases, resulting in a dispersion $\omega_k = c\sqrt{k^2 + 1/r_0^2(t)}$. As argued above, this is indeed supported by the two-step scaling behavior demonstrated above. Furthermore, at long times, we have $1/(2\eta) \ll 2$, therefore $n_v \propto g \propto t^2$, as observed in Fig. 3D.

In Fig. 4, we plot the experimental observations together with the RG flow diagram of Eqs.

1 and 2. For this representation, we define $x = 1/(2\eta) - 1/(2\eta_c)$ and $y = \sqrt{2}\pi g$. This ensures $x_c = 0$ at $\eta = \eta_c$ independent of system sizes, where $\eta_c = 0.13(1)$ for our finite-sized system and $\eta_c = \eta_{\mathrm{BKT}} = 1/4$ is the theoretical prediction in the thermodynamic limit. Our results follow a universal trajectory in the flow diagram. The quenched system begins at large x, where vortex excitations are suppressed and fugacity is small. Later on, non-equilibrium phonon creation drives the system towards smaller x, however still with suppressed y. As the system approaches the critical point $x_c = 0$, the onset of vortex excitation drives the transition.

Our work provides a comprehensive understanding of non-equilibrium dynamics across the BKT transition. The experimental measurements support the real-time RG picture of the universality out of equilibrium indicating that it is an excellent starting point for the theoretical study of a wide range of many-body dynamics within the framework of RG. The results also show that our matter-wave interference technique is ideally suited for further in-depth investigation of universal dynamics in 2D systems, such as the Kibble-Zurek scaling (*8*) and non-thermal fixed points (*39*).

References

1. T. Langen, *et al.*, *Science* **348**, 207 (2015).

2. T. Schweigler, *et al.*, *Nature* **545**, 323 (2017).

3. H. P. Zahn, *et al.*, *Phys. Rev. X* **12**, 021014 (2022).

4. T. Kinoshita, T. Wenger, D. S. Weiss, *Nature* **440**, 900 (2006).

5. W. H. Zurek, *Nature* **317**, 505 (1985).

6. I. Chuang, R. Durrer, N. Turok, B. Yurke, *Science* **251**, 1336 (1991).

7. S. L. Veatch, O. Soubias, S. L. Keller, K. Gawrisch, *PNAS* **104**, 17650 (2007).

8. T. W. B. Kibble, *J. Phys. A: Math. Theor.* **9**, 1387 (1976).

9. Q. Zhou, T.-L. Ho, *Phys. Rev. Lett.* **105**, 245702 (2010).

10. A. Polkovnikov, K. Sengupta, A. Silva, M. Vengalattore, *Rev. Mod. Phys.* **83**, 863 (2011).

11. J. Eisert, M. Friesdorf, C. Gogolin, *Nature Physics* **11**, 124 (2015).

12. N. Navon, A. L. Gaunt, R. P. Smith, Z. Hadzibabic, *Science* **347**, 167 (2015).

13. L. W. Clark, L. Feng, C. Chin, *Science* **354**, 606 (2016).

14. J. Beugnon, N. Navon, *J. Phys. B: At. Mol. Opt. Phys.* **50**, 022002 (2017).

15. A. Keesling, *et al.*, *Nature* **568**, 207 (2019).

16. M. Prüfer, *et al.*, *Nature* **563**, 217 (2018).

17. S. Erne, R. Bücker, T. Gasenzer, J. Berges, J. Schmiedmayer, *Nature* **563**, 225 (2018).

18. J. A. P. Glidden, *et al.*, *Nature Physics* **17**, 457 (2021).

19. L. Mathey, A. Polkovnikov, *Phys. Rev. A* **81**, 033605 (2010).

20. H.-C. Chu, G. A. Williams, *Phys. Rev. Lett.* **86**, 2585 (2001).

21. A. J. Groszek, P. Comaron, N. P. Proukakis, T. P. Billam, *Phys. Rev. Research* **3**, 013212 (2021).

22. S. Sunami, *et al.*, *Phys. Rev. Lett.* **128**, 250402 (2022).

23. V. Berezinskiĭ, *Sov. J. Exp. Theor. Phys.* **34**, 610 (1972).

24. J. M. Kosterlitz, D. J. Thouless, *J. Phys. C Solid State Phys.* **6**, 1181 (1973).

25. D. R. Nelson, J. M. Kosterlitz, *Phys. Rev. Lett.* **39**, 1201 (1977).

26. Z. Hadzibabic, P. Krüger, M. Cheneau, B. Battelier, J. Dalibard, *Nature* **441**, 1118 (2006).

27. See Supplementary Materials for more details.

28. L. Mathey, K. J. Günter, J. Dalibard, A. Polkovnikov, *Phys. Rev. A* **95**, 053630 (2017).

29. For the range of parameters used in this work, the ratio T/T_0 has a one-to-one mapping to the peak phase-space density of the trapped gas and sufficiently represents the effect of the quench; see Supplementary Materials.

30. A. J. Barker, *et al.*, *New J. Phys* **22**, 103040 (2020).

31. T. L. Harte, *et al.*, *Phys. Rev. A* **97**, 013616 (2018).

32. A. J. Barker, *et al.*, *J. Phys. B: At. Mol. Opt. Phys.* **53**, 155001 (2020).

33. We analyze the fringes within a region of interest corresponding to 80 % of the Thomas-Fermi radius of the quasi-condensate. As shown in the Supplementary Fig. S3, this is where the interference fringes are clear and allow reliable measurements.

34. I. Boettcher, M. Holzmann, *Phys. Rev. A* **94**, 011602 (2016).

35. In fact, a combined fitting function can be used that has power-law behavior at short distances and exponential scaling a long distances, where the exponential length scale can be infinite.

36. P. Comaron, F. Larcher, F. Dalfovo, N. P. Proukakis, *Phys. Rev. A* **100**, 033618 (2019).

37. To motivate the scaling regimes, we consider a linear spectrum $\omega_k = ck$. With this dispersion, dynamical phase factors of the form $\exp(i\omega_k t)$ are kept invariant, if a $z = 1$ scaling

is applied that leaves ckt invariant. Furthermore, for a spectrum that includes an additional length r_0, such as $\omega_k = c\sqrt{k^2 + 1/r_0^2(t)}$, for long times, only the modes with $\omega \approx c/r_0(t)$ contribute to the dynamics. Here the scaling is replaced by keeping $ct/r_0(t)$ fixed, as it was demonstrated for the long-time dynamics in Fig. 2C. As discussed in the main text and shown in Fig. 4, the length scale $r_0(t)$ is related to the vortex fugacity increasing at long times.

38. X. G. Wen, *Quantum Field Theory of Many-Body Systems: From the Origin of Sound to an Origin of Light and Electrons* (Oxford University Press, 2010).

39. J. Schole, B. Nowak, T. Gasenzer, *Phys. Rev. A* **86**, 013624 (2012).

40. S. Sunami, *et al.*, Dataset for "Universal scaling of the dynamic BKT transition in quenched 2D Bose gases" (2023).

41. K. Luksch, *et al.*, *New J. Phys.* **21**, 073067 (2019).

42. M. Holzmann, M. Chevallier, W. Krauth, *Phys. Rev. A* **81**, 043622 (2010).

43. E. Bentine, *et al.*, *Phys. Rev. Research* **2**, 033163 (2020).

44. N. Prokof'ev, B. Svistunov, *Phys. Rev. A* **66**, 043608 (2002).

45. C. L. Hung, X. Zhang, N. Gemelke, C. Chin, *Nature* **470**, 236 (2011).

46. Z. Hadzibabic, P. Krüger, M. Cheneau, S. P. Rath, J. Dalibard, *New J. Phys.* **10**, 045006 (2008).

47. R. J. Fletcher, *et al.*, *Phys. Rev. Lett.* **114**, 255302 (2015).

48. M. Holzmann, M. Chevallier, W. Krauth, *Eur. Phys. Lett.* **82**, 30001 (2008).

49. P. Krüger, Z. Hadzibabic, J. Dalibard, *Phys. Rev. Lett.* **99**, 040402 (2007).

50. A. Posazhennikova, *Rev. Mod. Phys.* **78**, 1111 (2006).

51. J. B. Kogut, *Rev. Mod. Phys.* **51**, 659 (1979).

52. T. Giamarchi, *Quantum Physics in One Dimension*, International Series of Monographs on Physics (Clarendon Press, Oxford, 2003).

53. J. M. Kosterlitz, *J. Phys. C: Solid State Phys.* **7**, 1046 (1974).

54. V. P. Singh, C. Weitenberg, J. Dalibard, L. Mathey, *Phys. Rev. A* **95**, 043631 (2017).

Acknowledgements

We acknowledge discussions with Junichi Okamoto on theoretical analysis and thank John Chalker for comments on our manuscript. **Funding:** The experimental work was supported by the EPSRC Grant Reference EP/S013105/1. S. S. acknowledges the Murata scholarship foundation, Ezoe foundation, Daishin foundation and St Hilda's College, Oxford for financial support. D. G., A. B., A. J. B. and K. L. thank the EPSRC for doctoral studentships. L. M. acknowledges funding by the Deutsche Forschungsgemeinschaft (DFG) in the framework of SFB 925 – project ID 170620586 and the excellence cluster 'Advanced Imaging of Matter' - EXC 2056 - project ID 390715994. V.P.S. acknowledges funding by the Cluster of Excellence 'QuantumFrontiers' - EXC 2123 - project ID 390837967. **Author contributions:** S.S. performed the experiments and data analysis. V.P.S. and L.M. developed numerical and analytical models and contributed to the interpretation of our experimental data. S.S. and V.P.S. wrote the manuscript. L.M. and C.J.F. supervised the project. All authors contributed to the discussion and interpretation of our results. **Competing interests:** The authors declare no competing interests. **Data and materials availability:** All data presented in this paper is available on Zenodo (*40*).

This research was funded in whole, or in part, by EPSRC Grant Reference EP/S013105/1, a Plan S funder.

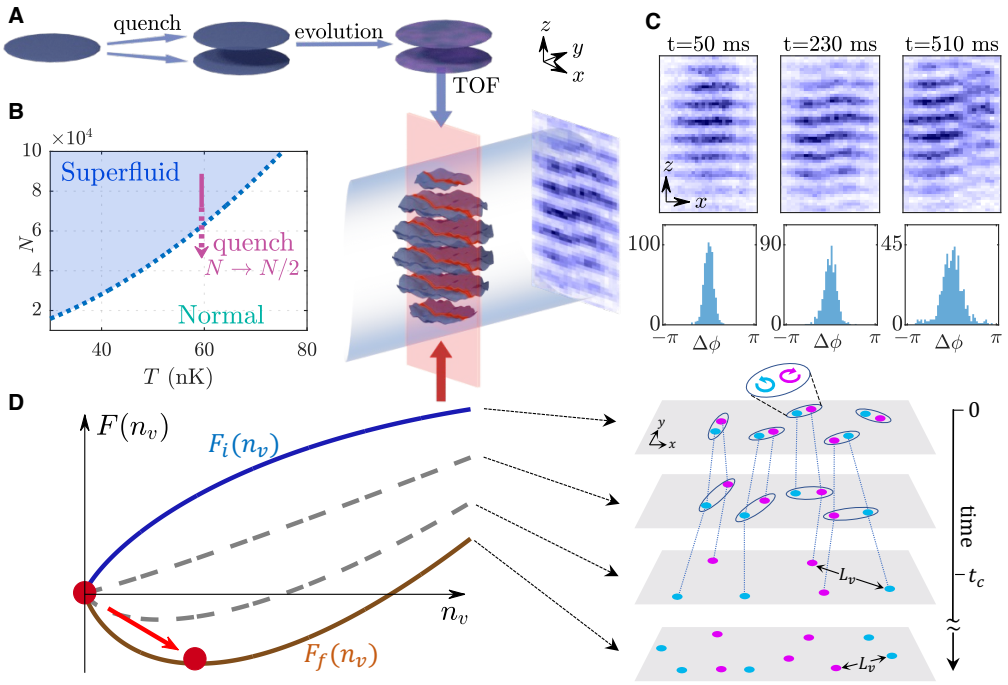

Figure 1: **Observation of non-equilibrium dynamics in 2D Bose gases via matter-wave interferometry.** (**A**) A 2D superfluid is split into two daughter clouds, thereby quenching through the BKT transition. The two clouds evolve for time t and are released to produce matter-wave interference after a time-of-flight (TOF). Local phase fluctuations are observed by optically pumping the slice (red sheet) and then performing absorption imaging. (**B**) Equilibrium phase-diagram of trapped 2D Bose gases (*27*). The quench forces the system out of equilibrium towards the normal phase. (**C**) Examples of interference images (top). Phase dislocation caused by a vortex is visible in the image at 510ms. The histograms (bottom) show the phase differences $\Delta\phi = \phi(x) - \phi(x')$ at $|x - x'| = 5\,\mu$m from 45 experimental runs. The decreasing height and increasing width indicate increased phase fluctuations. (**D**) (left) Free energies $F_i(n_v)$ and $F_f(n_v)$ (continuous lines) in equilibrium, for the initial and final conditions of the quench with their minima indicated by red points (*38*). Following the quench, the system relaxes towards the state with nonzero free vortex density n_v. (right) Illustration of the dynamics showing the transition between a scale-invariant phase supported by bound vortex-antivortex pairs and the broken scale-invariant phase characterized by free vortices with the mean vortex-vortex distance L_v where t_c is the crossover time.

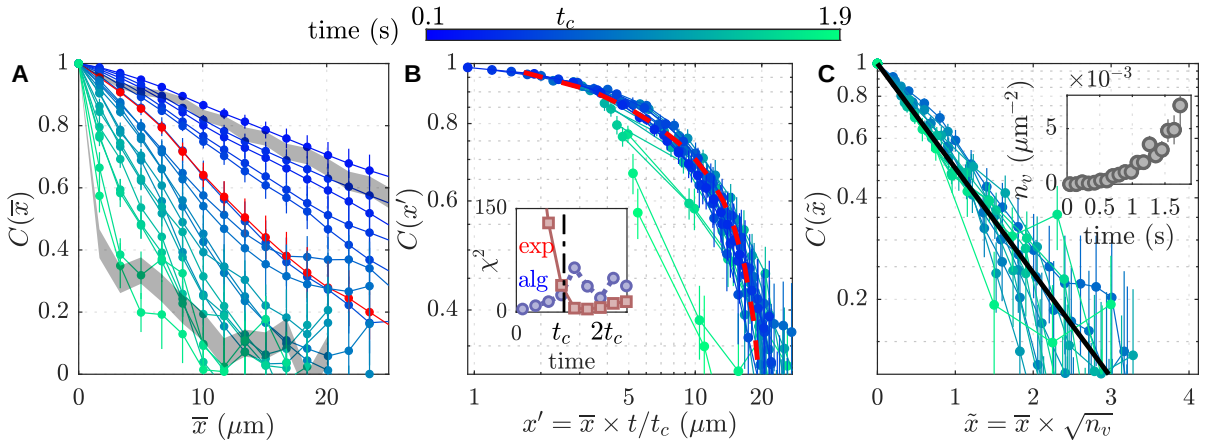

Figure 2: **Non-equilibrium scaling dynamics of the correlation function.** (**A**) Relaxation dynamics of the phase correlation function $C(\overline{x})$ measured after the quench for the initial reduced temperature $\tilde{T} = 0.34$, where $C(\overline{x})$ is an average over 45 realizations or more, and the error bars denote standard error. The data immediately after the critical time t_c is indicated by the red curve. For comparison, measured data for equilibrium 2D gases (*22*) are shown by the gray curves: $\tilde{T} = 0.41$ (top) in the superfluid regime and $\tilde{T} = 0.61$ (bottom) in the normal regime. (**B**) Linear scaling of length $x' = \overline{x}t/t_c$ according to time t/t_c results in a collapse towards a common curve for time evolution up to $t \sim 1$ s. This universal function is compatible with the expected behavior at the crossover in equilibrium (red dashed line), including the effect of inhomogeneity (*27*). At long times, deviations are observed (green points), indicating the breaking of scale invariance. Inset shows the χ^2 values for the algebraic and exponential fit functions (*27*). (**C**) Rescaling of the distance $\tilde{x} = \overline{x}\sqrt{n_v(t)}$ according to the vortex density $n_v(t)$ results in a collapse of the curves for times $t > 1$ s. Scaling behavior is compatible with an exponential decay (black solid line). Inset shows $n_v(t)$.

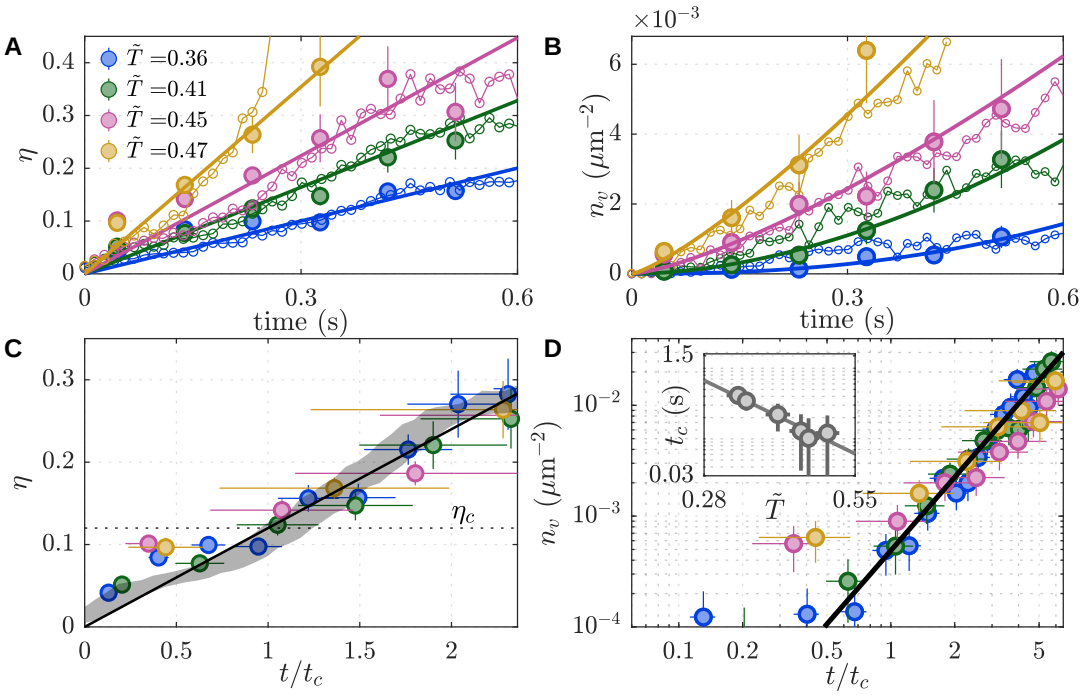

Figure 3: **Universal behavior across the dynamic BKT transition.** (**A**) Measured algebraic exponent $\eta(t)$ after the quench at different initial $\tilde{T}$ (filled circles), where the equilibrium critical temperature $\tilde{T}_c = 0.53$ is crossed by the quench (*22*). Open circles are the corresponding simulation results. Solid lines are linear fits to the experimental data and error bars denote standard fit errors. (**B**) Time evolution of the measured (filled circles) and simulated (open circles) vortex density $n_v(t)$. The solid lines are power-law fits to the experimental data. Error bars are statistical, given by the square root of observed vortex number. (**C**) Time evolution $\eta(t/t_c)$ scaled according to the $\tilde{T}$-dependent crossover time t_c. The horizontal error bars arise from the uncertainty in t_c. This universal behavior is used to determine the critical exponent $\eta_c = 0.13(1)$ (horizontal dotted line) at $t/t_c = 1$. The gray shaded curve indicates the simulation result at $\tilde{T} \sim 0.4$ and the solid line is a guide to the eye. (**D**) Scaled time evolution $n_v(t/t_c)$, plotted on a log-log scale, displays a universal growth after t_c. Black solid line is the fit with power-law $n_v \propto t^{2\nu}$ which yields $\nu = 1.1(1)$. The inset shows the dependence of t_c on $\tilde{T}$ with a solid line as a guide to the eye.

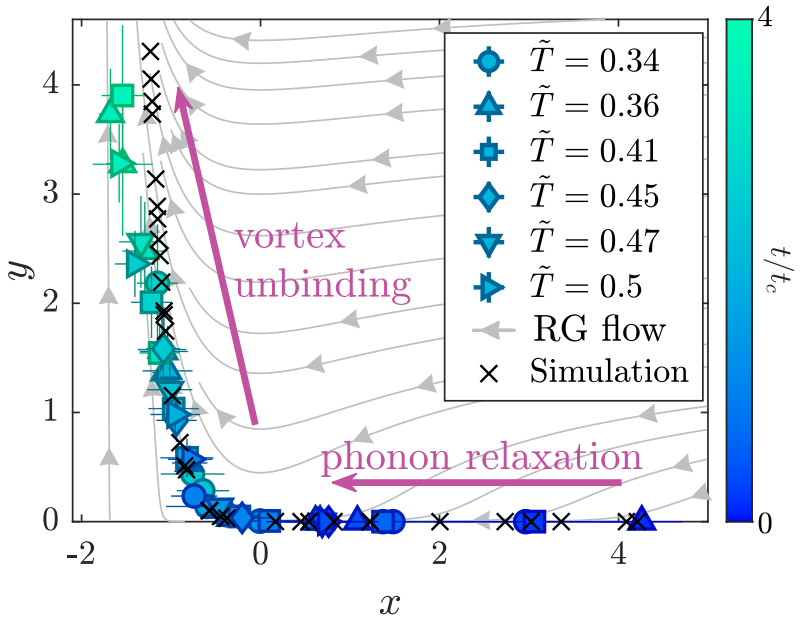

Figure 4: **Real-time renormalization group flow and measurements.** Gray lines with arrows are the RG flow of the parameters $x = 1/(2\eta) - 1/(2\eta_c)$ and $y = \sqrt{2}\pi g$; see Eqs. (1) and (2) and Ref. (*27*). These are compared with the experimental data for six different initial temperatures, with the time scaled by the corresponding $\tilde{T}$-dependent crossover time t_c. Error bars denote standard errors propagated from the values for η and n_v. The results from a numerical simulation at $\tilde{T} = 0.47$ are shown as black crosses, where the deviation from experimental data at small x is attributed to the slow trap-induced heating (*27*).

Supplementary Materials

Materials and Methods

Figs. S1 to S9

References (*41–54*)

Preparation of non-equilibrium 2D systems

We begin with an ultracold Bose gas of approximately 9×10^4 $^{87}\mathrm{Rb}$ atoms in the $F = 1$ hyperfine ground state, at temperatures $T = 40$ – 70 nK loaded adiabatically into a cylindrically symmetric, single-well quasi-2D potential as described in detail in Refs. (*31, 41, 43*). The trap is created by a multiple-radiofrequency-dressed potential (*22, 30*) with three RF components (f_1, f_2, f_3) = (7.14, 7.2, 7.26) MHz. The static quadrupole field $\boldsymbol{B}(\boldsymbol{r}) = b(x\boldsymbol{e}_x + y\boldsymbol{e}_y - 2z\boldsymbol{e}_z)$ has field gradient of $b = 145\,\mathrm{G\,cm^{-1}}$. The single-well potential has anisotropic confinement for radial and axial directions $\omega_r/2\pi = 13$ Hz and $\omega_z/2\pi = 1$ kHz, experimentally determined by the measurement of dipole oscillation in the trap. These experimental conditions give the dimensionless 2D interaction strength $\tilde{g} = \sqrt{8\pi}a_s/\ell_0 = 0.076$, where a_s is the 3D scattering length and $\ell_0 = \sqrt{\hbar/(m\omega_z)}$ is the harmonic oscillator length along z for an atom of mass m. These parameters satisfy a quasi-2D condition $k_BT \lesssim \hbar\omega_z$ for the parameters used in this paper: the presence of small excited state populations in the z direction at $\hbar\omega_z \sim k_BT$ results in a small reduction of the 2D interaction strength by $\sim 15\%$ (*48*) however this changes the BKT critical temperature by less than 4 % as a result (*42, 47*). We perform thermometry of the system before the quench (in equilibrium) in the single-well, by measuring the radial expansion of the far wings of density distribution following the release from the trap (*22*).

After holding the gas for 400 ms in the single trap (*22, 26*), we split the cloud into two daughter clouds by changing the vertical trap geometry from single- to double-well potential over 12 ms, thereby splitting the gas as illustrated in Fig. 1A and Fig. S1. This duration is chosen to be much shorter than the typical timescale for the radial dynamics $\sim 2\pi/\omega_r \sim 80$ ms. Following the splitting, each well confines $N \sim 4.5 \times 10^4$ atoms and final vertical trap frequency is $\omega_z/2\pi = 1\,\mathrm{kHz}$ for both trap minima, satisfying the quasi-2D condition. We ensure equal population of the two wells by maximizing the measured contrast of matter-wave interference patterns. Shortly before the splitting, we change the radial trapping frequency to $\omega_r/2\pi = 11\,\mathrm{Hz}$ by the change of b over 10 ms; this prevents the quench from exciting the monopole (radial breathing) mode by matching the radial density profiles before and after the splitting as much as is possible. This process, as well as the splitting procedure, are performed with duration much longer than characteristic timescale for the atomic motion in the vertical direction, $\tau_{\mathrm{trap}} \sim 2\pi/\omega_z \sim 1$ ms such that the system remain 2D. Following the splitting, the static quadrupole field has field gradient of $b = 94\,\mathrm{G\,cm^{-1}}$. We confirmed that there is no heating from the splitting procedure itself, by measuring the expansion dynamics before and after splitting, of a cloud above quasicondensation point (*22*), which gives the same temperature within uncertainties. The spatial separation of the double-well is $d = 7\,\mu\mathrm{m} \gg \ell_0$, which ensures the decoupling of the two clouds for the temperature range and trap parameters used in this work. The speed of sound in the 2D Bose gas is given by $c = \hbar\sqrt{n\tilde{g}}/m \sim 0.5\,\mu\mathrm{m\,ms^{-1}}$.

Quench across the critical point

From our previous interferometric measurements of the first-order correlation function and vortex density for a system at equilibrium (*22*), we determine that the equilibrium BKT critical

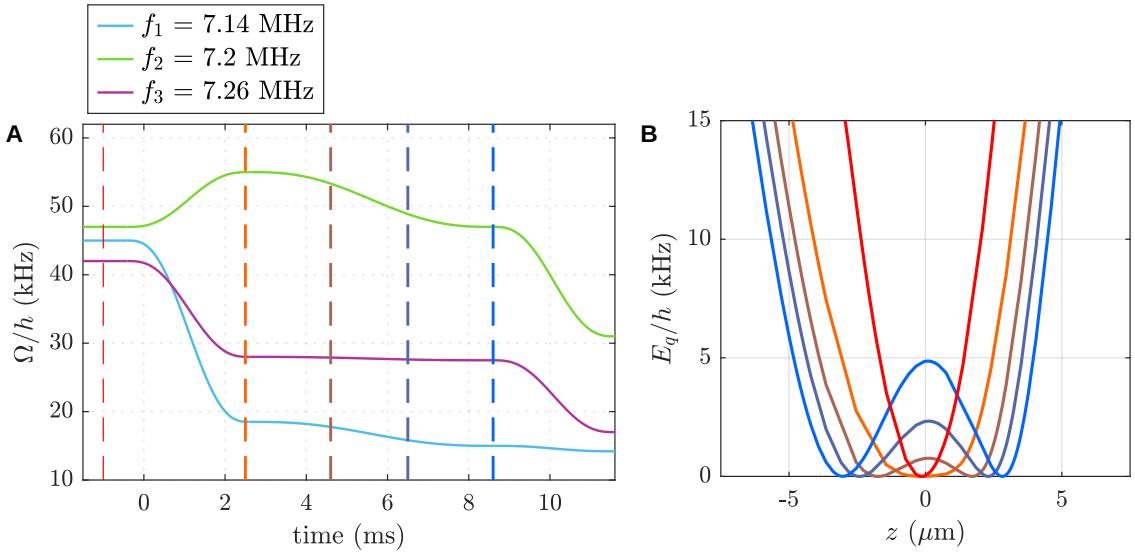

Figure S1: **The splitting procedure.** (**A**) The experimental procedure to transform the potential from single- to double-well. RF amplitudes are expressed in terms of Rabi frequencies $\Omega_i = g_F \mu_B B_i / 2\hbar$ for components $i = 1, 2, 3$, where B_i is the RF magnetic field amplitude at f_i, g_F is the Landé g-factor and μ_B the Bohr magneton. (**B**) The eigenenergy E_q for atoms in trapped dressed eigenstate $\tilde{m} = 1$, which form the trapping potential (*31*). We obtain position-dependent eigenenergies E_q using the Floquet numerical simulation (*31, 43*) for the static field gradient b and RF amplitudes Ω_i for each RF components $i = 1, 2, 3$ and the plotted potentials include the effect of gravity which acts in the direction of $-\boldsymbol{e}_z$. The red curve indicates the trap before the splitting sequence and the times for other colors are indicated by vertical dashed lines with corresponding colors in the left panel. The position z is defined relative to the center of the trap. To realise 2D confinements for the two wells $\omega_z/2\pi = 1\,\mathrm{kHz}$, we further modify the trap shape following the complete decoupling of the two wells (9-11.5 ms in left panel).

temperature is $\tilde{T}_{c,\mathrm{eq}} = 0.53(1)$ for the parameters used in this work: trap frequencies, interaction strength and atom number. Thus, the initial conditions of the system $\tilde{T}$ is chosen to satisfy $\tilde{T} \lesssim \tilde{T}_{c,\mathrm{eq}}$ and $\tilde{T}_f \gtrsim \tilde{T}_{c,\mathrm{eq}}$, where the value after the quench, $\tilde{T}_f \sim 1.67\tilde{T}$, is higher because of the change of atom number and radial trapping frequency. $\tilde{T}$ has a one-to-one mapping to the peak phase-space density $\mathcal{D} = n\lambda^2$, where $\lambda = h/\sqrt{2\pi m k_B T}$ is the thermal de Broglie wavelength, of the trapped gas as shown below. Thus $\tilde{T}$ can be used to identify whether the system should lie in the superfluid regime of the BKT transition if the system was in equilibrium, with $\tilde{T}_{c,\mathrm{eq}}$ being the critical value.

To demonstrate the mapping, we have obtained the theoretical predictions of density distribution in a harmonic trap by the application of classical-field simulation results in Ref. (*44*) for uniform systems to inhomogeneous systems within the local density approximation (LDA). The applicability of LDA in this method was confirmed by experiments in Ref. (*45*) for the

range of interaction strengths which includes the value we use. To complement the simulation in (*44*) which was performed only in the fluctuation region around the superfluid critical point, we have used the Hartree-Fock prediction (*46*) deep in the normal regime (*45*). These predictions smoothly connect at local phase-space density $\mathcal{D} \sim 2.5$ to give the complete density distribution.

In Fig. S2, we show the peak PSD for various atom numbers and temperature in 2D harmonic trap. The peak PSD depends only on the reduced temperature $\tilde{T}$, confirming the description above. At $\tilde{T} = \tilde{T}_{c,\mathrm{eq}}$, the peak PSD is ~ 20, as observed in Ref. (*22*). The phase diagram in equilibrium (Fig. 1B) was also obtained using this method and gives the phase boundary $\tilde{T} = \tilde{T}_{c,\mathrm{eq}}$ on the $T - N$ plane. We note that, as studied in Refs. (*47, 48*), the ideal-gas condensation, which accompanies the divergence of peak PSD (*48*), is suppressed at the interaction strength used in this work and we can neglect its effect on the dynamics (*47*).

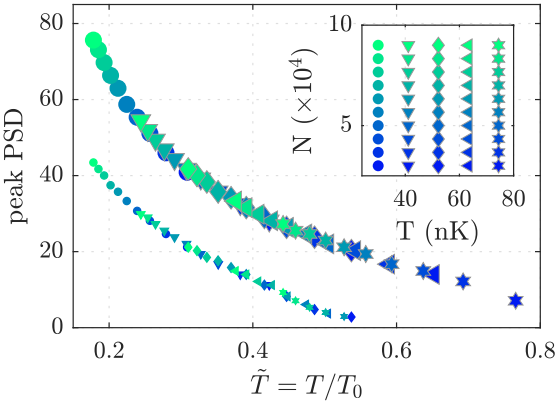

Figure S2: **Phase-space density (PSD) as a function of the reduced temperature $\tilde{T}$.** The peak PSD of harmonically-trapped 2D gases in equilibrium are plotted for $\omega_r/2\pi = 13$ Hz for the temperatures and atom numbers indicated by the symbols and colors on the inset. Points with smaller markers represent the peak PSD we expect after the quench from the initial parameters indicated by larger markers.

Image analysis

After variable time t following the quench, we abruptly turn off the trap and image matter-wave interference patterns with a spatially-selective repumping technique to obtain the local fluctuation of relative phases, as described in detail in Ref. (*22*). In this method, we apply a spatially-modulated laser beam that optically pumps a thin slice through the cloud of atoms from $F = 1$ hyperfine state to $F = 2$, which we subsequently detect by absorption imaging. The repumping beam is a thin sheet of thickness $L_y = 5\,\mu\mathrm{m}$, which goes through the centre of the cloud and the sheet is normal to the imaging light, as illustrated in Fig. 1A.

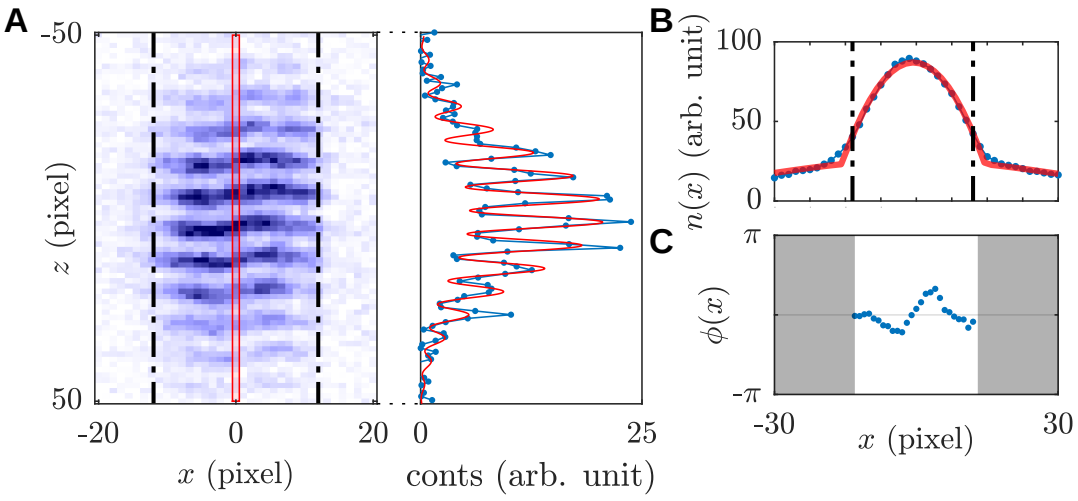

Figure S3: **Interference analysis and region of interest.** (**A**) An example of interference image recorded after the quench, where pixel size in the image plane corresponds to $\ell_{\rm pixel} = 1.67\,\mu$m. The density distribution along the pixel column $x = 0$ is shown on the right with the fitted curve (red). (**B**) Density distribution recorded after the TOF, integrated along z. Red line denotes the fit with the bimodal model Eq. S1. Dash-dotted lines indicate the 80% of the central Thomas-Fermi peak, which is also shown in **A** and corresponds to the region where clear interference fringes are observed. (**C**) Obtained phase profile $\phi(x)$ from the fits at each pixel column x. We only analyze the phases within 80% of the central peak.

In the images, the density distributions along x (the radial density distribution, obtained by integrating the image along z) are bimodal, with a narrow central Thomas-Fermi density profile (inverted parabola) and a broad thermal cloud with Gaussian profile, as observed in equilibrium (*22, 49*). It is within the central Thomas-Fermi distribution that interference fringes are clearly observed. The observed density distribution, integrated along z, is fitted well with the bimodal model

$$f(x) = n_{\rm TF}\max(0, 1 - r^2/R^2) + n_{\rm Th}e^{-r^2/2\sigma_n^2}, \tag{S1}$$

where $n_{\rm TF}, R, n_{\rm Th}, \sigma_n$ are the fit parameters, as shown in Fig. S3B. During the TOF with duration $t_{\rm TOF} \ll 2\pi/\omega_r \sim 100$ ms that we use in the experiments, σ_n increase due to the ballistic expansion of the thermal component while the Thomas-Fermi peak shows negligible expansion and R stays constant. For the density distribution along z direction, we evaluate the phase profile $\phi(x)$ of interference patterns by fitting the column density distributions at each pixel column x with

$$f(z) = n_p \exp\left(-z^2/2\sigma^2\right)\left[1 + c_0\cos(kz + \phi)\right], \tag{S2}$$

where $n_p, \sigma, c_0, k, \phi$ are the five fit parameters (see Fig. S3A; red box in the left panel shows the distribution that is being fitted on the right panel) and we perform the fit at each x within

the 80% of the Thomas-Fermi region of the cloud as illustrated in Fig. S3A: for each image, we repeat the fitting at varying x (red box shown in Fig. S3A). The obtained phase profiles $\phi(x)$, such as shown in Fig. S3C, encodes the *in situ* relative phases of two gases along a line that goes through the centre (*22*) and reveals the phase fluctuation in non-equilibrium 2D systems. This would no longer hold for systems with a much shorter correlation length r_0 than L_y but from the parameters used in this work and measurement results in equilibrium (*22*), we expect the system to satisfy $L_y \ll r_0$. Further details of the phase correlation analysis is described in detail in (*22*). To obtain the atom number N, we repeat measurements with a large repumping beam that covers the entire density distribution following TOF. The detectivity of the absorption imaging for the measurement of N was calibrated using the known Bose-Einstein condensation critical point of 3D gases, as described in detail in (*22*).

Phase correlation function

At each time and initial condition, we make $N_r = 45$ observations of fringes to measure the spatial phase fluctuations. We compute the phase correlation function $C(x - \overline{x}/2, x + \overline{x}/2)$ as defined in the main text and average over x where both $x - \overline{x}/2$ and $x + \overline{x}/2$ fall within the 80 % of the Thomas-Fermi peak of the density distribution along x. The region of interest for the correlation analysis is defined so that we analyze the phase data only within 80% of the Thomas-Fermi peak of the density distribution (*22*). In Fig. S4, we show the time evolution of correlation functions at three temperatures to demonstrate the robustness of the universal behaviour reported in the main text (Fig. 2).

The extraction of η in the inhomogeneous 2D system relies on the local correlation approximation (LCA) (*34*), which is the local density approximation of the correlation properties in the system. We have previously demonstrated the applicability of LCA on the phase correlation function of 2D Bose gases in equilibrium, in Ref. (*22*) by comparing to experimentally observed phase correlation functions. Essentially, the LCA in Ref. (*34*) amounts to the replacement of η with a position-dependent one, resulting in the first-order correlation function in the superfluid regime of the form $g_1(\boldsymbol{r}, \boldsymbol{r}') \propto |\boldsymbol{r} - \boldsymbol{r}'|^{-\eta n_0/\sqrt{n(\boldsymbol{r})n(\boldsymbol{r}')}}$ where $n(\boldsymbol{r})$ is the 2D density at location $\boldsymbol{r}$ and n_0 is the peak density. To fit the spatially averaged phase correlation function $C(\overline{x})$, we define $\tilde{n}(x - \overline{x}/2, x + \overline{x}/2) = \sqrt{n(x - \overline{x}/2)n(x + \overline{x}/2)}$ and average over x within the 80 % of the Thomas-Fermi peak to obtain $\tilde{n}(\overline{x})$. We then fit the correlation function $C(\overline{x})$ with $f_{\text{alg}}(\overline{x}) = a\overline{x}^{-2\eta\alpha(\overline{x})}$ with $\alpha(\overline{x}) = \frac{\max(\tilde{n}(\overline{x}))}{\tilde{n}(\overline{x})}$ where a and η are fit parameters. The obtained η represents the averaged value within the region of interest (*22*). We use this model to obtain the expected correlation function at the crossover in equilibrium, shown in Fig. 2B, for $\eta = \eta_c = 0.13$ and assuming Thomas-Fermi density distribution of the form $n(x) = \max(0, 1 - x^2/R^2)$ with $R = 25\,\mu\text{m}$ which is close to the experimental values of R.

We further fit $C(\overline{x})$ with $f_{\text{exp}}(\overline{x}) = be^{-2\overline{x}/r_0}$, which models the correlation function decay deep in the normal regime of the BKT transition; in the normal regime, the correlation length is typically shorter than the slow variation of inhomogeneous density within the analysis region and we expect almost purely exponential behaviour as we have shown using numerical simu-

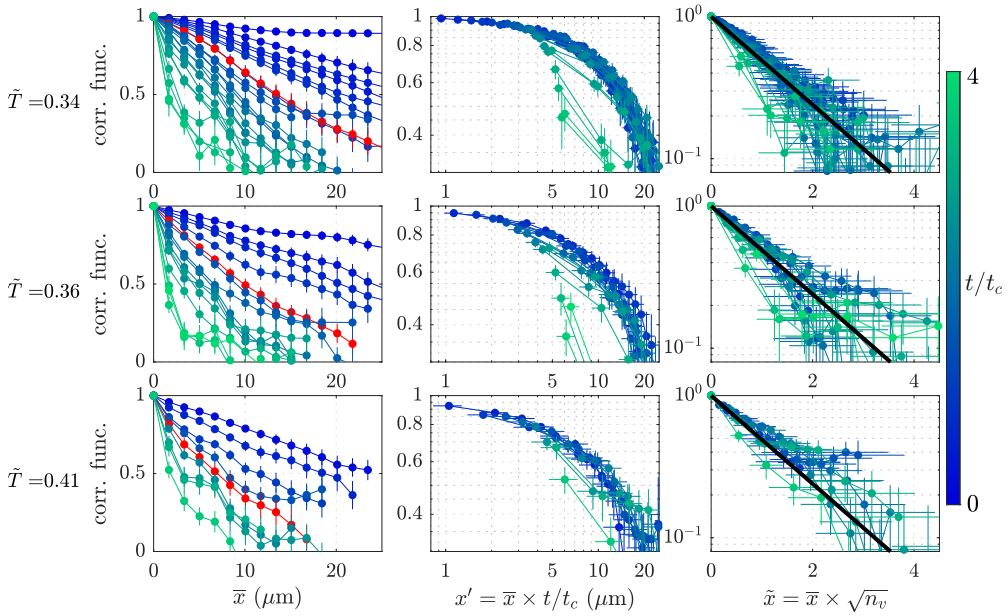

Figure S4: **Correlation function and scale-invariant behavior.** The left column shows the correlation functions at times ranging from 0 s to $4t_c$, where t_c are the temperature-dependent crossover time. Because of the smaller region used for the correlation analysis (performed within Thomas-Fermi region with temperature-dependent size), bottom left panel shows smaller number of data points. Middle column shows the rescaled correlation functions in which we perform the rescaling of the distance by $x' = \overline{x}t/t_c$, in the same way as Fig. 2B. Also as for Fig. 2B, we exclude data at $t < 200$ ms for this plot, which are affected by the initialization of the relative phase in the coherent splitting and expected to deviate from the universal behavior. We include here the horizontal error bars that arise from the uncertainties of t_c. Finally, right panels show the correlation functions in the crossover to normal regime ($t > t_c$), with distance scaled by the mean vortex-vortex distance $1/\sqrt{n_v}$. Black solid line is the exponential function (same as Fig. 2C) to guide the eye and horizontal error bars originate from uncertainties of n_v.

lation in Ref. (*22*). Since r_0 cannot exceed the system size, the value of r_0 is bounded by the TF diameter, the approximate system size where BKT physics is observed (*50*). From fits of measured $C(\overline{x})$ with $f_{\rm alg}$ and $f_{\rm exp}$ and the uncertainties of the data points, we obtain the χ^2 statistic which describes the goodness of fit; lower χ^2 values indicate better fit. χ^2 values that are too low, such as $\chi^2 < 4$ for the degree of freedom for the fits performed in this work, indicate incorrect estimation of errors rather than a better fit however the χ^2 values we obtained are comfortably above this threshold. At short times, $\chi^2_{\rm alg}$ is lower than $\chi^2_{\rm exp}$ however as the system evolves towards the normal regime, $\chi^2_{\rm exp}$ becomes lower than $\chi^2_{\rm alg}$, shown in Fig. 2B inset as an example. We determine the crossover time, at which the correlation function become better described by the exponential model, from the crossover of $\chi^2_{\rm alg}$ and $\chi^2_{\rm exp}$. For the typical degree of freedom for the fit procedure, a model is accepted if $\chi^2 \lesssim 40$ at 5% level of significance.

The functional form of correlation functions across the non-equilibrium BKT crossover

For a system at thermal equilibrium, the BKT transition can be viewed in the RG picture as process that sweeps across fixed points of the RG flow corresponding to different initial conditions (*25*). This case assumes equilibration, at infinite time, and gives a sharp transition: the fixed points for $T < T_c$ correspond to complete suppression of vortices, while for $T > T_c$ the fixed points have a large vortex fugacity corresponding to complete unbinding of vortex pairs.

The non-equilibrium case studied here is distinctly different in nature; within the *real-time* RG picture the time evolution is not limited to the fixed points (*28*). From a non-equilibrium initial condition, the system follows the real-time RG flow as time progresses, eventually reaching a fixed point after long evolution time. As such, the physical picture is different from that for a system at equilibrium and only at times $t = 0$ and $t \to \infty$ is there a direct correspondence with equilibrium theory. During the critical dynamics, the system evolves smoothly from power-law to exponential correlation functions as the vortex-antivortex pairs unbind (*19*). We fit the correlation functions with power-law and exponential functions and use the χ^2 statistic to identify the characteristic time at which the correlations become better described by an exponential function. However, the power-law model and an analysis based on the values of η is expected to be valid even after time t_c, since vortex excitations are yet to completely destroy the algebraic order of the system especially at shorter length scales compared to typical vortex separations. Indeed, while the power-law model gives worse fits than exponential models for $t > t_c$, the χ^2 values remain comparable with the value at 5 $\%$ threshold even for longer times $t > t_c$. Complete breakdown of the power-law description of the correlation functions (and rapid increase of the errors of fitted values of η) is typically observed for $t \gtrsim 3t_c$ for our system.

Checking the consistency of scaling in Fig. 2B and Fig. 3C

According to Fig.2B, within the scale-invariant regime the correlation function $C(\overline{x}, t)$ should have the form

$$C(\overline{x}, t) \sim C_1(x') = (x')^{-\eta_c}, \tag{S3}$$

up to $t \sim 2t_c$, where $x' = \overline{x}t/t_c$. At the same time, the linear increase of η in Fig. 3C implies that

$$C(\overline{x}, t) \sim C_2(\overline{x}, t) = \overline{x}^{-\eta_c t/t_c}. \tag{S4}$$

To show that these two expressions are consistent, we define a function that is the ratio

$$f_c(\overline{x}, t) = \frac{C_1(x')}{C_2(\overline{x}, t)} = \overline{x}^{\eta_c(t/t_c - 1)} \left(\frac{t}{t_c}\right)^{-\eta_c}, \tag{S5}$$

for $t/t_c \in [0, 2]$. The time evolution of this function is plotted in Fig. S5 and shows that $f_c(\overline{x}, t)$ is close to unity for the values of $\overline{x}$ relevant for our experiment; the experimental measurements of $C(\overline{x})$ typically have an uncertainty of $\sim 15\%$, and we find that the consistency of scaling demonstrated in Figs. 2B and 3C holds around the critical time, $|t - t_c| \lesssim 0.7t_c$.

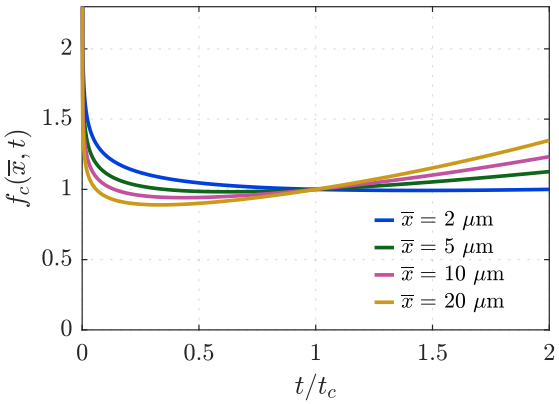

Figure S5: **The consistency of the scaling in the power-law regime.** The time evolution of the function $f_c(r,t)$ defined in Eq. (S5) times $t/t_c \in [0,2]$ at various lengths r.

Vortex detection

The method used to obtain the vortex density from the interference patterns is described in detail in Ref. (*22*), which improves upon the method used in Ref. (*26*) and takes advantage of the selective imaging method to obtain the vortex density; vortices are only detected when they lie within the density slice region, and allows the analysis of vortex density by dividing the probability of detecting vortices in interference patterns by the well-defined detection area, as demonstrated in equilibrium by comparing to the classical-field simulation (*22*). To identify vortices, we look for sudden jumps of phase $\phi(x)$, and obtain n_v from their occurrences in $N_r = 45$ experimental repeats. In Ref. (*22*), we found good agreement of the vortex density in equilibrium across the BKT transition, with the values obtained from the extensive classical-field predictions performed with the same parameters as in the experiment. To confirm this further for the non-equilibrium case, we plot in Fig. S6 C the correlation length r_0 against $1/\sqrt{n_v}$; since the mean vortex distance $1/\sqrt{n_v}$ determines the correlation length in the normal regime, we expect $r_0 = 1/\sqrt{n_v}$. The experimental data points are consistent with this prediction, further confirming our vortex detection method. In Fig. 3D, we set the lower bound of the vertical axis at $10^{-4}\mu\mathrm{m}^{-2}$. This is because observing only a single vortex in the dataset typically results in $n_v \sim 0.9 \times 10^{-4}\mu\mathrm{m}^{-2}$ where statistical uncertainty is large and n_v fluctuates between zero and finite value.

Real-time RG equations

In Ref. (*19, 28*), the dynamical sine-Gordon model of the form

$$\mathcal{L} \sim \frac{\tau}{8\pi}\Big[-\frac{(\partial_t\theta)^2}{2c^2} + \frac{(\partial_x\theta)^2}{2}\Big] + \frac{g}{a^2}\cos\theta \tag{S6}$$

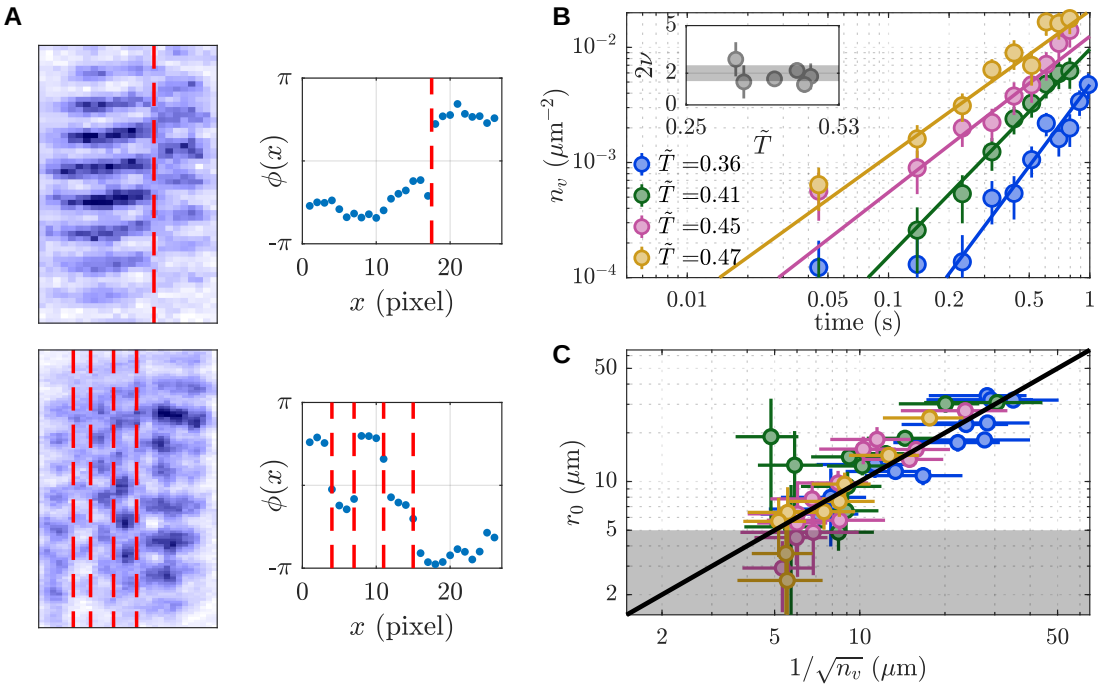

Figure S6: **Vortex detection and correlation length.** (**A**) Vortices are detected by sudden phase jumps such as those shown in the leftmost panels for single and multiple vortices at locations indicated by the red dashed lines. The adjacent panels show the phase distributions. (**B**) Time evolution of the vortex density n_v (circles) and the corresponding power law fit $t^{2\nu}$ (continuous line) are shown for different initial reduced temperature $\tilde{T}$, which are the same as in Fig. 3B. Inset shows the obtained exponent 2ν with a shaded region as a guide to the eye. (**C**) Correspondence of the correlation length r_0 extracted by an exponential fitting of the correlation function $C(\overline{x})$ and the vortex density. The black solid line is the predicted relationship $r_0 = 1/\sqrt{n_v}$ (*38*). The black shaded region denotes $r_0 < 5\,\mu$m where the extraction of r_0 is unreliable because $C(\overline{x})$ rapidly decays towards 0 within a few datapoints.

was studied, as a dual model describing the BKT transition. As derived in Ref. (*19*), the dynamical renormalization group (RG) equations are

$$\frac{dg}{d\ell} = \left(2 - \frac{2}{\tau}\right) g, \tag{S7}$$

$$\frac{d\tau}{d\ell} = \frac{\pi^2 g^2}{\tau}. \tag{S8}$$

These equations describe the relaxation dynamics of the system at long times. ℓ is the flow parameter, related to real time by $t = t_0 e^{\ell}$ and non-universal constant of the RG equation in (*28*) is set so that the numerical prefactor for Eq. S8 is unity. These flow equations coincide with the flow equations for the static system in equilibrium, see e.g. (*51, 52*). While the flow equations of

the static system identify which ordered state the system forms, and what the critical properties of the equilibrium phase transition are, the dynamical flow equations describe the universal many-body dynamics across the transition. Written in terms of the time t and $\eta = \tau/4$, they are

$$\frac{dg}{dt} = \left(2 - \frac{1}{2\eta}\right)\frac{g}{t}, \tag{S9}$$

$$\frac{d\eta}{dt} = \frac{\pi^2 g^2}{16\eta t}. \tag{S10}$$

To motivate these flow equations, we consider the quantity $\langle|\theta_{k,0}|^2 \cos^2 \omega_k t\rangle$, which contributes to the fluctuations of the real-valued field $\theta(r,t)$, the dual field describing the BKT transition in the sine-Gordon model (*19*). For a linear spectrum $\omega_k = ck$, and for times $t \ll 1/(ck)$, the quantity acts like a static quantity with its initial value. For $t \gg 1/(ck)$, the quantity is dephased to a new near-static quantity, that acts as a slowly varying correction for the low-energy modes with $ck \ll 1/t$. This motivates the $z = 1$ scaling that keeps ckt invariant. The inverse time $1/t$ acts as a cut-off on the mode dynamics of the field, which motivates the analogy to equilibrium renormalization flow, in which a momentum cut-off is lowered to improve the low-energy model. At the time t, the modes with $\omega_k \approx 1/t$ undergo the dephasing dynamics, acting as a renormalization on the other degrees of freedom. The non-linear term $\sim g\cos\theta$ takes the modes that undergo the dephasing into account. For η increasing above the critical value, the term becomes relevant, generating an additional length r_0, that enters the dispersion as $\omega_k = c\sqrt{k^2 + 1/r_0^2(t)}$. This dynamical emergence of the length scale r_0 indicates the dynamical phase transition.

The time evolution of the vortex fugacity is suppressed if the scaling exponent η is smaller than the critical value $\eta_{\rm BKT}$, and increases rapidly if $\eta > \eta_{\rm BKT}$. As mentioned in the main text, a finite-size system might be characterized by a modified value of $\eta_c < \eta_{\rm BKT}$. The magnitude of η is increased by vortex-antivortex unbinding, corresponding to the g^2 contribution. As mentioned in the main text, we introduce a phenomenological heating rate γ, to model the heating due to technical noise:

$$\frac{dg}{dt} = \left(2 - \frac{1}{2\eta}\right)\frac{g}{t}, \tag{S11}$$

$$\frac{d\eta}{dt} = \frac{\pi^2 g^2}{16\eta t} + \gamma, \tag{S12}$$

In the analysis presented in the main text, we use $x = 1/(2\eta) - 2$ and $y = \sqrt{2}\pi g$ which is similar to the form used by Kosterlitz in Ref. (*53*) for equilibrium RG theory of BKT transition. The resulting RG equations are

$$\frac{dy}{dt} = -\frac{xy}{t}, \tag{S13}$$

$$\frac{dx}{dt} = -\frac{(x+2)^3 y^2}{8t} - 2\gamma(x+2)^2. \tag{S14}$$

For $\gamma = 0$, we find the conserved quantity $x^2 - y^2 = \text{const.}$ near the critical point $x \sim 0$, which allowed the visual inspection of critical behavior in Ref. (*53*). The phenomenological term γ, added in Eq. S12, models the finite heating of the system in the trap. In Fig. S7 A, we compare the measured heating in the system with the expected heating in the theoretical model due to our phenomenological term γ: from Eq. S12 with the assumption of $g \ll 1$, we find the expected temperature of the system using the linear relationship of η and system temperature in the superfluid regime $\eta \sim \zeta T$ where $\zeta = 4 \times 10^{-3}\ \mathrm{nK}^{-1}$, observed in equilibrium with the same trap parameters, interaction strength and similar atom number (*22*). We find reasonable agreement of the measured heating in the trap with the parameter that we use, $\gamma = 0.02\,\mathrm{s}^{-1}$. In Fig. 4, to incorporate the finite-size effect which shifts the critical algebraic exponent, we use $x = 1/(2\eta) - 1/(2\eta_c)$ with $\eta_c = \eta_{\mathrm{BKT}} = 1/4$ for theoretical curves and $\eta_c = 0.13(1)$ for experiments, which results in $x_c = 0$ at $\eta = \eta_c$ independent of the system size.

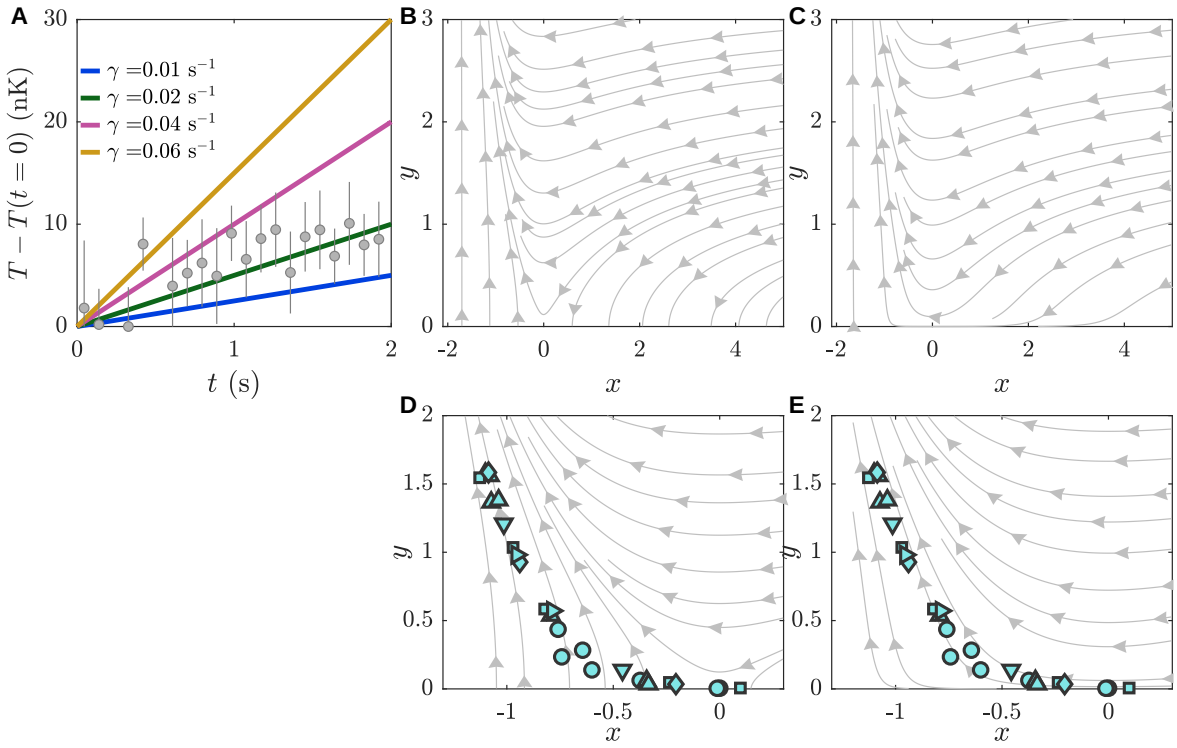

Figure S7: **The effect of the finite heating on the RG flow.** (**A**) The points represent the measured heating in the trap. Lines are the heating described by the term γ by solving Eq. S12 with $\eta(t=0) = 0$ and assuming $g \ll 1$, at different values of γ. **(B,C)** The RG flow diagram plotted for $\gamma = 0$ (B) and $\gamma = 0.02\,\mathrm{s}^{-1}$ (C). **(D,E)** RG flow diagram for $\gamma = 0$ and $\gamma = 0.02\,\mathrm{s}^{-1}$, together with experimental data shown in Fig. 4.

The advantage of direct comparison on the RG flow diagram, as performed in Fig. 4, is that no concrete initial conditions and timescales are required to compare the theoretical predictions

with the experimental findings. To obtain Fig. 4, we find the vortex fugacity g using (*38*)

$$n_v(t) = \xi^{-2} \exp\left(\frac{2\ln(g/2)}{2 - 1/(2\eta)}\right), \tag{S15}$$

where $\xi \sim 1\,\mu\mathrm{m}$ is the healing length of the system which we obtain from the mean density of the system n by $\xi = 1/\sqrt{n\tilde{g}}$. From Eq. S15, $n_v \propto g$ for large η and thus supports $n_v \sim g \sim t^2$ in the main text. In Fig. S7 B and C, we compare the RG flow diagrams with $\gamma = 0$ and $\gamma = 0.02\,\mathrm{s}^{-1}$.

Scaling for vortex unbinding dynamics

To demonstrate the predicted scaling of the vortex unbinding dynamics $n_v \propto t^2$, we first numerically solve Eqs. S7 and S8 and obtain the results for the time evolution of vortex density. We plot the results in Fig. S8 for initial conditions $\eta_0 \in [0.05, 0.25]$ with initial vortex fugacity $g_0 = 0.01$ (*19*).

Furthermore, as an approximate solution of Eq. S12, we assume $\eta(t) = \eta_0 + \gamma t$, which is a linear behavior in time as observed in Fig. 3A and 3C. With this time dependence of $\eta(t)$, the flow equation S11 has the analytic solution

$$g(t) = g_0\left(\frac{t}{t_0}\right)^{2-1/(2\eta_0)}\left(\frac{\eta_0 + \gamma t}{\eta_0 + \gamma t_0}\right)^{1/(2\eta_0)} \tag{S16}$$

with the initial value $g(0) = g_0$. The long-time limit displays the $\sim t^2$ behavior:

$$g(t) = g_0(t/t_0)^2\left(\frac{\gamma t_0}{\eta_0 + \gamma t_0}\right)^{1/(2\eta_0)} \tag{S17}$$

The vortex density behaves as

$$n_v(t) = \frac{1}{\xi^2}\left(\frac{g_0}{2}\right)^{\frac{2}{2-\frac{1}{2\eta(t)}}}\left(\frac{t}{t_0}\right)^{\frac{2-\frac{1}{2\eta_0}}{2-\frac{1}{2\eta(t)}}}\left(\frac{\eta_0 + \gamma t}{\eta_0 + \gamma t_0}\right)^{\frac{1}{2\eta_0}\frac{2}{2-\frac{1}{2\eta(t)}}} \tag{S18}$$

for $\eta(t) = \eta_0 + \gamma t > 1/4$. The long time behavior displays t^2 scaling:

$$n_v(t) \sim \frac{1}{\xi^2} g_0\left(\frac{t}{t_0}\right)^2\left(\frac{\gamma t_0}{\eta_0 + \gamma t_0}\right)^{\frac{1}{2\eta_0}} \tag{S19}$$

At short times, the time dependence deviates from the t^2 behavior, similar to the numerically integrated result shown in Fig. S8.

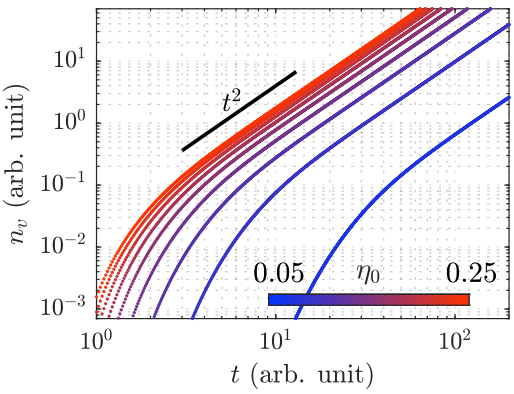

Figure S8: **Vortex scaling.** Time evolution of n_v obtained by numerical integration of the real-time RG equations S9, S10. The slope of solid black line indicates the power-law scaling t^2 which all the curves follow at long time.

Classical-field simulations

We simulate the dynamics of two-dimensional (2D) Bose gases using the classical-field method of Ref. (*54*). The initial system is described by the Hamiltonian

$$\hat{H}_i = \int d^2\mathbf{r} \left[\frac{\hbar^2}{2m} \nabla\hat{\psi}^\dagger(\mathbf{r}) \cdot \nabla\hat{\psi}(\mathbf{r}) + V(r)\hat{\psi}^\dagger(\mathbf{r})\hat{\psi}(\mathbf{r}) + \frac{g_{2D}}{2}\hat{\psi}^\dagger(\mathbf{r})\hat{\psi}^\dagger(\mathbf{r})\hat{\psi}(\mathbf{r})\hat{\psi}(\mathbf{r}) \right], \tag{S20}$$

where $\hat{\psi}$ ($\hat{\psi}^\dagger$) is the bosonic annihilation (creation) operator, m is the atomic mass, and $g_{2D} = \tilde{g}\hbar^2/m$ is the 2D interaction parameter. $V(r) = m\omega_r^2 r^2/2$ describes the harmonic trap potential, where ω_r is the trap frequency and $r = (x^2 + y^2)^{1/2}$ is the radial coordinate. We choose the total atom number $N = 9 \times 10^4$, $\omega_r/2\pi = 13\,\mathrm{Hz}$ and $\tilde{g} = 0.076$, which are the same as the experiments. For numerical simulations we discretize space on a lattice with discretization length $l = 0.5\,\mu\mathrm{m}$. In our methodology we replace the operators $\hat{\psi}$ in Eq. S20 and in the equations of motion by complex numbers ψ. We sample the initial states from a grand-canonical ensemble of a chemical potential μ and a temperature T_i via a classical Metropolis algorithm. This corresponds to the initial cloud of the experiment.

To imitate coherent splitting of the initial cloud into two clouds, we consider a second state ψ_2 and initialize it with quantum fluctuations (*28*). We then use a $\pi/2$-pulse rotation as a quench to initialize non-equilibrium states ψ_1 and ψ_2 with equal densities, in a similar manner to the method employed in Ref. (*28*). Following the quench, ψ_1 and ψ_2 evolve under the equations of

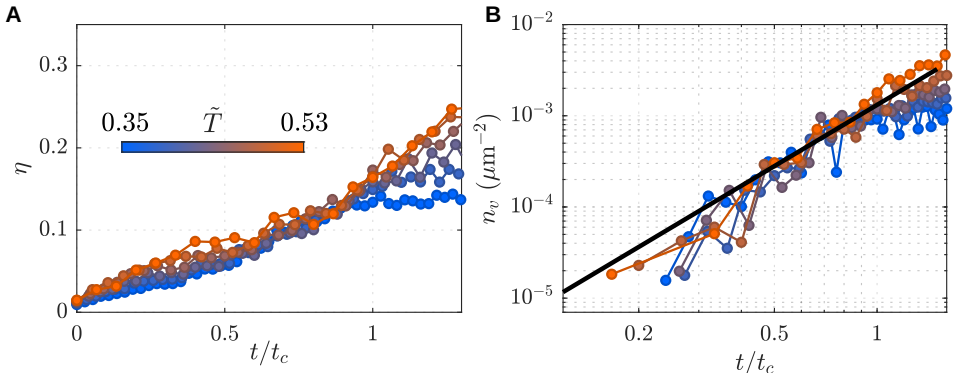

Figure S9: **Universal scaling from numerical simulation.** (**A**) Time evolution of algebraic exponent against rescaled time t/t_c, with temperature-dependent crossover time t_c. (**B**) Time evolution of vortex density n_v. Black solid line is the fit with power-law scaling $n_v \propto t^{2\nu}$, which yields $\nu = 1.1(1)$.

motion

$$i\hbar\frac{\partial\psi_1}{\partial t} = \left(-\frac{\hbar^2}{2m}\nabla^2 + V(r) + g_{2D}|\psi_1|^2\right)\psi_1 + J_t\psi_2, \tag{S21}$$

$$i\hbar\frac{\partial\psi_2}{\partial t} = \left(-\frac{\hbar^2}{2m}\nabla^2 + V(r) + g_{2D}|\psi_2|^2\right)\psi_2 + J_t\psi_1, \tag{S22}$$

where we have added a time-dependent tunneling term $J_t = J\exp(-t/t_0)$ to account for nonzero coupling of the clouds during and shortly after the splitting. $J = \hbar^2/(2ml^2)$ is the single-particle tunneling energy. We set $t_0 = 60\,\mathrm{ms}$ to capture the rapid decoupling dynamics of the experiment after the splitting. We use $\omega_r/2\pi = 11\,\mathrm{Hz}$, which is the same as in the experiment, and calculate the time evolution of $\psi_1(t)$ and $\psi_2(t)$ to analyze the dynamics after the quench at $t = 0$. From the arguments of complex numbers $\psi_1(t)$ and $\psi_2(t)$, we calculate the relative-phase correlation function and the vortex density, in the same way as the experiment, with the effect of density slicing, and average over the initial ensemble. The initial temperature T_i is chosen to be close to the experimental temperature. In Fig. S9, we plot the time evolution of η and n_v against the rescaled time t/t_c where t_c is the temperature-dependent crossover time, obtained from the simulation data. We note that the simulation method does not include the effect of slow trap-induced heating, and result in the deviation from experimental results at long times when the heating effect becomes sizeable as we observe for small x in Fig. 4.